72

SATELLITE & MESOMETEOROLOGY RESEARCH PROJECT

Department of the Geophysical Sciences
The University of Chicago

AERIAL MEASUREMENT OF RADIATION TEMPERATURES OVER MT. FUJI AND TOKYO AREAS AND THEIR APPLICATION TO THE DETERMINATION OF GROUND- AND WATER-SURFACE TEMPERATURES

by

Tetsuya Fujita and Gisela Baralt
The University of Chicago

and

Kiyoshi Tsuchiya
Japan Meteorological Agency

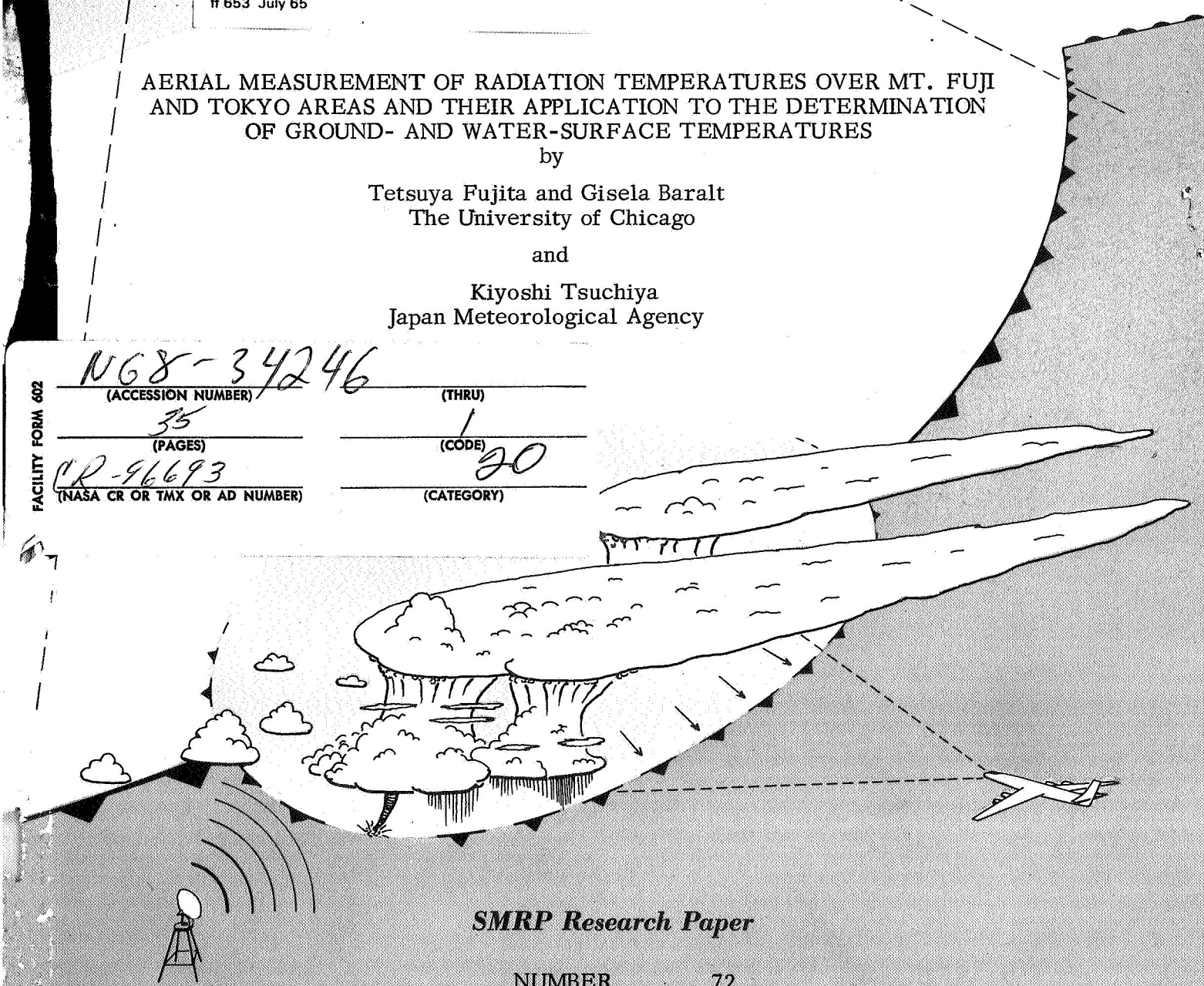

SMRP Research Paper

NUMBER 72

March 1968

MESOMETEOROLOGY PROJECT --- RESEARCH PAPERS

1.* Report on the Chicago Tornado of March 4, 1961 - Rodger A. Brown and Tetsuya Fujita

2.* Index to the NSSP Surface Network - Tetsuya Fujita

3.* Outline of a Technique for Precise Rectification of Satellite Cloud Photographs - Tetsuya Fujita

4.* Horizontal Structure of Mountain Winds - Henry A. Brown

5.* An Investigation of Developmental Processes of the Wake Depression Through Excess Pressure Analysis of Nocturnal Showers - Joseph L. Goldman

6.* Precipitation in the 1960 Flagstaff Mesometeorological Network - Kenneth A. Styber

7.** On a Method of Single- and Dual-Image Photogrammetry of Panoramic Aerial Photographs - Tetsuya Fujita

8. A Review of Researches on Analytical Mesometeorology - Tetsuya Fujita

9. Meteorological Interpretations of Convective Nephsystems Appearing in TIROS Cloud Photographs - Tetsuya Fujita, Toshimitsu Ushijima, William A. Hass, and George T. Dellert, Jr.

10. Study of the Development of Prefrontal Squall-Systems Using NSSP Network Data - Joseph L. Goldman

11. Analysis of Selected Aircraft Data from NSSP Operation, 1962 - Tetsuya Fujita

12. Study of a Long Condensation Trail Photographed by TIROS I - Toshimitsu Ushijima

13. A Technique for Precise Analysis of Satellite Data; Volume I - Photogrammetry (Published as MSL Report No. 14) - Tetsuya Fujita

14. Investigation of a Summer Jet Stream Using TIROS and Aerological Data - Kozo Ninomiya

15. Outline of a Theory and Examples for Precise Analysis of Satellite Radiation Data - Tetsuya Fujita

16. Preliminary Result of Analysis of the Cumulonimbus Cloud of April 21, 1961 - Tetsuya Fujita and James Arnold

17. A Technique for Precise Analysis of Satellite Photographs - Tetsuya Fujita

18. Evaluation of Limb Darkening from TIROS III Radiation Data - S.H.H. Larsen, Tetsuya Fujita, and W.L. Fletcher

19. Synoptic Interpretation of TIROS III Measurements of Infrared Radiation - Finn Pedersen and Tetsuya Fujita

20. TIROS III Measurements of Terrestrial Radiation and Reflected and Scattered Solar Radiation - S.H.H. Larsen, Tetsuya Fujita, and W.L. Fletcher

21. On the Low-level Structure of a Squall Line - Henry A. Brown

22. Thunderstorms and the Low-level Jet - William D. Bonner

23. The Mesoanalysis of an Organized Convective System - Henry A. Brown

24. Preliminary Radar and Photogrammetric Study of the Illinois Tornadoes of April 17 and 22, 1963 - Joseph L. Goldman and Tetsuya Fujita

25. Use of TIROS Pictures for Studies of the Internal Structure of Tropical Storms - Tetsuya Fujita with Rectified Pictures from TIROS I Orbit 125, R/O 128 - Toshimitsu Ushijima

26. An Experiment in the Determination of Geostrophic and Isallobaric Winds from NSSP Pressure Data - William Bonner

27. Proposed Mechanism of Hook Echo Formation - Tetsuya Fujita with a Preliminary Mesosynoptic Analysis of Tornado Cyclone Case of May 26, 1963 - Tetsuya Fujita and Robbi Stuhmer

28. The Decaying Stage of Hurricane Anna of July 1961 as Portrayed by TIROS Cloud Photographs and Infrared Radiation from the Top of the Storm - Tetsuya Fujita and James Arnold

29. A Technique for Precise Analysis of Satellite Data, Volume II - Radiation Analysis, Section 6. Fixed-Position Scanning - Tetsuya Fujita

30. Evaluation of Errors in the Graphical Rectification of Satellite Photographs - Tetsuya Fujita

31. Tables of Scan Nadir and Horizontal Angles - William D. Bonner

32. A Simplified Grid Technique for Determining Scan Lines Generated by the TIROS Scanning Radiometer - James E. Arnold

33. A Study of Cumulus Clouds over the Flagstaff Research Network with the Use of U-2 Photographs - Dorothy L. Bradbury and Tetsuya Fujita

34. The Scanning Printer and Its Application to Detailed Analysis of Satellite Radiation Data - Tetsuya Fujita

35. Synoptic Study of Cold Air Outbreak over the Mediterranean using Satellite Photographs and Radiation Data - Aasmund Rabbe and Tetsuya Fujita

36. Accurate Calibration of Doppler Winds for their use in the Computation of Mesoscale Wind Fields - Tetsuya Fujita

37. Proposed Operation of Intrumented Aircraft for Research on Moisture Fronts and Wake Depressions - Tetsuya Fujita and Dorothy L. Bradbury

38. Statistical and Kinematical Properties of the Low-level Jet Stream - William D. Bonner

39. The Illinois Tornadoes of 17 and 22 April 1963 - Joseph L. Goldman

40. Resolution of the Nimbus High Resolution Infrared Radiometer - Tetsuya Fujita and William R. Bandeen

41. On the Determination of the Exchange Coefficients in Convective Clouds - Rodger A. Brown

* Out of Print
** To be published

(Continued on back cover)

SATELLITE AND MESOMETEOROLOGY RESEARCH PROJECT
Department of the Geophysical Sciences
The University of Chicago

AERIAL MEASUREMENT OF RADIATION TEMPERATURES OVER MT. FUJI AND TOKYO AREAS AND THEIR APPLICATION TO THE DETERMINATION OF GROUND- AND WATER-SURFACE TEMPERATURES

by

Tetsuya Fujita and Gisela Baralt
The University of Chicago

and

Kiyoshi Tsuchiya
Japan Meteorological Agency

SMRP Research Paper No. 72
March 1968

The research reported in this paper has been sponsored by ESSA (MSL) under Grant Cwb WBG-34 and NASA under Grant NsG 333. The portion of the research performed in Japan was supported by US-Japan cooperative science program under NSF GF-255 and JSPS GEO-19.

AERIAL MEASUREMENT OF RADIATION TEMPERATURES OVER MT. FUJI AND TOKYO AREAS AND THEIR APPLICATION TO THE DETERMINATION OF GROUND- AND WATER-SURFACE TEMPERATURES[1]

by

Tetsuya Fujita and Gisela Baralt
The University of Chicago

and

Kiyoshi Tsuchiya
Japan Meteorological Agency

ABSTRACT

A Barnes PRT-4 portable radiometer with a spectral response in the 8-14 micron range was used to determine the equivalent blackbody temperature of (1) the slope of Mt. Fuji, (2) Sagami Bay, and (3) the city of Tokyo. A twin-engine aircraft was used to fly over these areas at various altitudes up to 12,000 ft. Through mapping the slope temperatures of Mt. Fuji, it was learned that the rocky slope heats up under the morning sun very rapidly to 32C almost irrespective of the elevation. The distribution of measured temperatures explains the reasons for the rapid growth of cumulus clouds along the east slope in the early morning hours. The nadir-angle and the height dependence of equivalent blackbody temperatures measured over Tokyo and Sagami Bay was examined. The measured temperatures were compared with those computed from the radiative transfer equation. It was found that the values over Tokyo are reproduced fairly well by the addition of a graybody smog filling the layers up to 910 mb. To express the effects of atmospheric radiation upon the reduction of the radiant emittance from the surface,

---

[1] The research reported in this paper has been sponsored by ESSA (MSL) under Grant Cwb WBG-34 and NASA under Grant NsG 333. The portion of the research performed in Japan was supported by US-Japan cooperative science program under NSF GF-255 and JSPS GEO-19.

a damping factor was introduced. The factor which designates the reduction of the amplitude of the surface temperature when measured from aircraft or satellites must be known to an accuracy of about 10% in order to estimate the true temperature variation or gradient from measured equivalent blackbody temperatures. Further investigation of the temperature damping is necessary to determine accurately the radiometric sea-surface temperature.

1. Introduction

As a result of the latest development in infrared radiometers which can be operated on board an aircraft or a satellite, their applications to meteorology are increasing rapidly. Combs et.al. (1965) made aerial measurements of ground and cloud temperatures by using Barnes R-4D1 industrial radiometers with a spectral response extending from 8 microns to beyond 32 microns and a model 14-310 radiometer with 8 to 13 micron spectral response. Their study showed that the emissivity of various types of soil exceeds 0.95, making it possible to assume the blackbody radiation at the surface for most practical purposes. The equivalent blackbody temperatures measured from an aircraft flying over Arizona showed a significant contribution of the atmosphere located beneath the flight level. A 18.5 C reduction of the desert temperature was obtained when measured from 10,500 ft and the reduction was only 4.6C when the radiometer was pointed toward the adjacent irrigated field. The atmosphere over the desert and the adjacent field may be regarded identical in terms of vertical distribution of temperature and moisture. In other words, the temperature difference of 26.2C between the desert (60.2C) and the field (34.0) was reduced to only 12.3C when measured from the 10,500 ft level.

Effects of atmospheric radiation in airborne measurements of surface temperature were estimated by Lenschow and Dutton (1964). Since their main concern was to measure surface temperatures from a low-flying airplane equipped with a radiometer of a 20° field of view, the measured radiation was separated into the energy from the ground and that from the atmosphere assumed to be of a uniform temperature. Then they obtained an equation for computing the surface temperature from the measured temperature, air temperature, and a parameter indicating the ratio of the increments in measured and air temperatures.

Despite the fact that the atmosphere beneath the flight level attenuates the outgoing radiation from the underlying surface while reradiating at its temperature, resulting sometimes in a significant difference between measured and actual temperatures, a window-channel radiometer can be used for indirect measurements of ground- or water-surface temperature from the air. Aerial measurements of the sea-surface by Lorenz (1967), for example, demonstrated the capability of detecting warm and cold spots as well as the thermal gradients on the sea surface.

Our radiation measurement over the Mt. Fuji and Tokyo areas was carried out by using a Barnes PRT-4 radiometer in an attempt to obtain the surface temperature of the city, the mountain, and a bay between them. Shown in Fig. 1 are the isolines of visibility contoured at 10-km intervals and the locations of Mt. Fuji, A; Sagami Bay, B; Tokyo, C; and the upper-air station at Tateno, D. The radiometric measurements were made from a twin-engine aircraft based at Haneda International Airport southwest of Tokyo. Five flights were made between 4 am and 6 pm on July 28, 1967.

2. Spatial and Spectral Responses of PRT-4

The Barnes PRT-4 is a portable radiometer with its output either read from an indicator dial or recorded with an EA recorder. We took advantage of both capabilities so that any change in measured temperature could be noticed immediately while obtaining a continuous record for later data reduction and analyses.

The field of view at the half-power point is 2 deg which would receive radiant emittance from a circular area 35-m in diameter when viewed straight down from 1000 m above the ground. The full-power field of view naturally extends much beyond the circle. Nevertheless, the hand-held operation permitted us to measure the radiation from relatively small areas such as bridges on rivers, playgrounds, railroad yards, etc.

The spectral response of the radiometer extends between 7.4 and 16.0 microns with an insignificant response near 19 microns. Presented in Fig. 2 is the distribution of the spectral response, ϕ_λ excluding that around 19 microns. The spectral radiant emittance of a blackbody, $B(\lambda,T)$ in watts $m^{-2}\mu^{-1}$ was computed at 10 C intervals between -20C and 50C to determine the spectral radiant emittance $W(\lambda,T)$ filtered by the radiometer's optical system. Figure 2 shows that the wave length giving rise to the maximum contribution shifts from 9.5 microns toward 12 microns as the black-

body temperature decreases to -20C.

The effective radiant emittance as defined by NASA (1961) was then computed from

$$\overline{W} = \int_0^\infty B_{(\lambda,T)} \phi_\lambda d\lambda \tag{1}$$

which denotes that portion of blackbody radiant emittance which would be detected by a sensor with a spectral response ϕ_λ when the field of view is completely filled with a unique temperature radiator. It should be noted that no atmospheric absorption is assumed to exist between the sensor and the blackbody radiator when $\overline{W}$ is computed as a function of temperature using Eq. (1). The result of computed $\overline{W}$ for the radiometer is shown in Fig. 3.

Although it is customary to use radiance in expressing the radiation flux reaching a radiation sensor we may multiply by π both sides of the radiation transfer equation as discussed by Greenfield and Kellogg (1960) to write

$$\overline{W} = \iint \phi_\lambda B_{(\lambda,T)} d\tau d\lambda + \int e_s \tau_{s\lambda} \phi_\lambda B_{(\lambda,T_s)} d\lambda \tag{2}$$

where τ denotes the transmissivity of the atmosphere from the sensor to any level and τ_s, to the background radiator with temperature, T_s and emissivity e_s. The first integral represents the contribution of the atmosphere and the second, that of the background. Although we may assume that $e_s = 1$, the measured effective radiant emittance expressed by Eq. (2) is not a unique function of T_s due to the influence of the atmosphere which would change the first integral as well as τ_s in the second integral.

In accordance with the definition by NASA (1961) we use the term, equivalent blackbody temperature, T_{BB} to designate the temperature obtained by equating Eqs. (1) and (2). Thus we obtain T_{BB} simply by converting measured effective radiant emittance into the corresponding temperature by using the curve in Fig. 3 or Eq. (1).

3. Slope Temperature of Mt. Fuji Heated by the Early Morning Sun.

A circular flight at 12,000 ft around Mt. Fuji was made shortly after sunrise on July 28, 1967. A hand-held radiometer scanned along four separate scan lines shown in Fig. 4. Each scan was completed in about two minutes leaving an inverted V-shaped scan line. The topography of the mountain soaring to 3776-m height is shown with contour lines drawn for every 500 m. The areas of rocks and sand distribute asymetrically down from the inactive crater at the top.

The recorded traces along two scan lines indicated by the letters A through E and F through N are reproduced in Fig. 5. The circled letters in Figs. 4 and 5 correspond to each other. The traces show that the equivalent blackbody temperature decreased from A to C as the scan spot moved upward along the western slope which was still in the shadow of the mountain. The rise in temperature from C to E took place almost symmetrically to the scan-up trace.

Of particular interest is the temperature trace obtained while scanning along the eastern slope which had been in the sun since 0446 JST, the sunrise time. As expected, the equivalent blackbody temperature dropped a few degrees while the scan spot advanced from F to G. Upon reaching a small area of rocks at H the temperature jumped by 13C then plunged down while crossing a narrow grassland separating the small rocky area from the main area of rocks and sand. From J to M, the temperature went up and down keeping a mean value of about 30C regardless of the elevation of the slope.

The distribution of the equivalent blackbody temperature on the mountain slope is presented in Fig. 6 which also includes the direction and the elevation angles of the sun between sunrise and the time of the radiometric measurement. It will be found that the temperature decreases with height over the slope regardless of the sunlit and the shadow sides, except over the rocky and sandy slope illuminated by the morning sun. There are two hot spots on the east slope. The one near the mountain top was probably due to the lesser atmospheric absorption of short-wave radiation and to the large angle between the slope and the incoming ray. The other at a lower elevation would be due to the lapse rate of the ambient atmosphere which resulted in a higher mean temperature during the night.

Two days earlier, on July 26, 1967 a series of near-infrared pictures was taken looking south from Funatsu Weather Station. The meteorological conditions around the mountain were almost a carbon copy of those on the day of our experiment. The pictures in Fig. 7 show that the cumulus clouds on the east slope became thicker and thicker between 0845 JST and 0917 JST when the elevation angle of the sun increased from 47 to 53 deg.

It would be desirable to obtain detailed meteorological data along the eastern slope while airborne measurements are being made. Even though no such attempt was made at this time, it was learned that the Japan Meteorological Agency (1958) had operated several network stations along the slope. From these data, we selected Aug. 18, 1952 which was very close in meteorological conditions to the day of our measurements, the time sections of clouds, winds, surface, and air temperatures shown in Fig. 8 were made. The locations of the stations numbered 1 through 5 appear in Fig. 4. All stations are approximately in line with the 110-deg azimuth from the highest station at 3775 m on the southwest rim of the crater. As seen in Fig. 8, the lowest station at 468 m was covered with stratus cloud during most of the dark hours. Only scattered to broken cumuli were reported following the sunrise. Station 2 at 1300 m located in a wooded area showed a gradual rise in the surface temperature. Due to the fact that the station was located just outside the rocks and sand area, it was in the cumulus base continuously between 9 and 18 JST. Stations 3, 4, and 5 located in the rocks and sand area showed a marked rise, as much as 30C, in the surface temperature. Cumulus formation took place over stations 3 (2780 m) and 4 (3240) suggesting that the patterns of cumulus along the slope would have been just like those presented in Fig. 7. It is of interest to find that the rise in the air temperature measured inside the instrument shelter was gradual amounting to only a few degrees without responding to the abrupt rise in the surface temperature.

Results of our radiometric measurement, infrared photography from Funatsu station, and network station data collected during past years revealed that the rocky slope of Mt. Fuji is heated very rapidly by the early morning sun while the shady slope remains cool during early morning hours. A significant heat source along the east slope early in the morning stimulates the cumulus formation, thus providing a natural laboratory for studies of orographic convection involving solar heating effects. It was found that the equivalent blackbody temperature measured from an aircraft is very useful in learning the mode of heating and cooling of the mountain slope with various radiative characteristics ranging from those of rocky and sandy slope to wooded ground at low levels.

4. Height and Nadir-Angle Dependence of the Equivalent Blackbody Temperature Measured over Land and Water

Two areas for aerial measurements of radiation were selected in order to study the effects of the height and the nadir angle in determining the equivalent blackbody temperatures by means of indirect sensing from the air. The first area selected was over the Sagami Bay (see Fig. 9) with approximately 26C sea-surface temperature. The area was relatively smog-free with surface visibility in excess of 20 km as shown in Fig. 1. The second area was selected over the western part of Tokyo covered with medium density smog reaching to 910 mb. A separate thin layer of smog was seen at about the 900-mb level (see Fig. 10).

During the radiation measurement the aircraft flew at a constant pressure altitude while the hand-held radiometer was raised from a minimum nadir angle of about 40 deg to a maximum of 100 deg. The observer's hand was placed momentarily in front of the radiometer when the scan spot crossed the apparent horizon. The angular velocity of the sensor was kept more or less constant manually so that the nadir angle of view can be obtained by dividing the recorded trace at uniform intervals. During the measurement at each height between 500 ft and 10,000 ft, the sensor was raised upward to 100 deg nadir angle followed by a return to the minimum nadir angle.

The equivalent blackbody temperatures obtained from altitudes 1000, 2000, 4000, 6000, 8000, and 10,000 ft were plotted and contoured in Fig. 11. Both the pressure and the pressure altitude of the aircraft appear along the right and the left sides. The nadir angle increases toward the right from 0 to 120 deg.

The contour lines drawn for the T_{BB} show that the measured value increases to a maximum of more than 26C when the aircraft altitude increases to about 2000 ft suggesting that the atmosphere below this level was warmer than the sea surface. By extrapolating the measured values down to the sea surface, the sea-surface temperature was estimated to be slightly less than 25C. After the completion of our radiometric measurement, it was learned that the sea-surface temperature beneath our flight path was about 26C according to direct measurements.

If we know the temperature and humidity distribution over the sea surface, it is feasible to compute the equivalent blackbody temperature as a function of pressure or pressure altitude and the nadir angle of view. Now we shall discuss the result of our computation made by using a 7094 computer at the University of Chicago.

In computing the radiance $N(\lambda,T)$ reaching the airborne detector by using the radiative transfer equation,

$$N_{(\lambda,T)} = \int_{\tau_0}^{1} \frac{B_{(\lambda,T)}}{\pi} d\tau + \frac{B_{(\lambda,T_s)}}{\pi} \tau \qquad (3)$$

and ϕ_λ the spectral response of PRT-4, we divided the spectral range between 7.4 and 16.0 microns (see Fig. 2) into 43 parts each with 0.2 - micron intervals. Then the transmissivity between the aircraft and a specific layer, either above or below the aircraft, was computed by dividing the atmosphere into 40 layers of 20 mb each located between 1010 mb at sea level and 210 mb.

Then we computed the effective optical path, u_e , given by

$$u_e = \frac{\sec \eta}{g} \int_{P_a}^{P} q \frac{P}{P_0} dP \qquad (4)$$

where P_a is the static pressure at the flight level, P_0 = 1000 mb; q, the mixing ratio; and η , the nadir angle of view.

For the window region between 8.1 and 12.9 microns, we used Wark, Yamamoto, and Lienesh's (1962) approach in which the transmissivity for a specific wave number or wave length is expressed as a function of u_e only. Outside the window region, we approximated the calculation by neglecting the temperature effect so as to use Elsasser's (1960) generalized absorption coefficient

$$\tau = f(u_e \cdot L) \quad . \qquad (5)$$

Because the spectral radiance on both sides of the window region will be reduced significantly by the spectral response of the PRT-4, we used the τ vs $u_e \cdot L$ relationship at P_0 = 1000, used by Wark et.al. (1962) in their computation.

Assuming the aircraft to be at the top of a layer for the convenience of computations, spectral transmissivities from the aircraft to either the bottom (when looking down) or the top (when looking up) of all 40 layers were calculated. After changing Eq. (3) into radiant emittance form,

$$W_\lambda = \int_{\tau_s}^{1} B_{(\lambda,T)}\, d\tau \;+\; B_{(\lambda,T_s)}\tau_s \tag{6}$$

in order to obtain T_{BB} from Eq. (1), we write it in difference form:

$$W_\lambda = \sum_{n=1}^{n=a} B_{(\lambda,T_n)}\Delta\tau_n \;+\; B_{(\lambda,T_s)}\tau_s \tag{7}$$

for the looking-down case and

$$W_\lambda = \sum_{n=a+1}^{n=b} B_{(\lambda,T_n)}\Delta\tau_n \tag{8}$$

for the looking-up case. The layer number n = 1 is assigned to the bottom layer, n = a, to the layer just below the aircraft, and n = b, the uppermost layer.

The effective radiant emittances for the looking-down and the looking-up cases are written respectively as

$$\overline{W} = \sum_{m=1}^{m=c}\sum_{n=1}^{n=a} \phi_\lambda B_{(\lambda_m,T_n)}\Delta\tau_n\Delta\lambda \;+\; \sum_{m=1}^{m=c} \phi_\lambda B_{(\lambda_m,T_s)}\tau_s\Delta\lambda \tag{9}$$

and

$$\overline{W} = \sum_{m=1}^{m=c}\sum_{n=a+1}^{n=b} \phi_\lambda B_{(\lambda_m,T_n)}\Delta\tau_n\Delta\lambda \tag{10}$$

where $\Delta\lambda = 0.2$ micron for this case. The effective radiant emittances computed from these equations were converted into equivalent blackbody temperatures from Eq. (1) or Fig. 3.

A computed result appears in Fig. 12 in which T_{BB} was plotted and contoured at 5C intervals with heavy lines and at 1C intervals with light lines. The input air temperatures are seen along the vertical through the 90-deg nadir angle at which the radio-

meter measures the temperature at the flight level because $\sec\eta$ in Eq. (4) reaches infinity. The maximum temperature, 27.6C at about 1000 ft above the 26.0C sea surface results in an increase in T_{BB} by a few tenths of a degree when the aircraft altitude increases to about 1000 ft. Above this altitude the T_{BB} decreases as the flight level increases.

Similar measurements were repeated over Tokyo on July 28, 1967. The city was covered with light to moderate smog reaching to about 910 mb (See Fig. 10). A separate thin layer was seen at the 900 mb level which was approximately the base of convective clouds. Few pieces of very low stratus clouds were located at about the 960-mb level. In our radiation measurements none of these clouds were scanned to avoid undesirable consequences. Measurements started at the 10,000-ft pressure altitude where the air was clean with extremely high visibility permitting us to see distant mountains to the west and north. The measured equivalent blackbody temperature dropped sharply when the sensor axis was raised beyond the apparent horizon. The first indication of smog at the flight level was felt when the aircraft descended from 4000 to 2000 ft. At the time of the sean from the 2000-ft level it was noticed that T_{BB} does not decrease as it did at the higher level s when the radiometer was pointed a few degrees above the apparent horizon. The response to the space background was much slower when measured from the 1000-ft altitude, the lowest flight altitude permitted over Tokyo. The result of measurements over Tokyo appear in Fig. 13 in which the smog-covered portions in the diagram are stippled.

In view of the existence of smog over Tokyo, it was attempted to compute equivalent blackbody temperatures taking the influence of smog into consideration. No satisfactory experimental data for such computations are available as far as Tokyo smog is concerned. Unlike the case of Los Angeles smog, residents rarely feel eye irritation in Tokyo although the smog reduces the visibility, resulting sometimes in a dim sun even in midday.

In our computation we assumed that the smog in question is a graybody within the spectral range of the PRT-4 radiometer. This assumption may not seem valid because the largest size of aerosols in the atmosphere is no larger than 10 microns. In their computation of visibility from the particle-size distribution, Rudolf, Pueschel, and Kenneth (1967) showed, however, that the concentration of large-size aerosols is one order of magnitude larger in an urban atmosphere than in a maritime atmosphere.

Barret and Ben-Dov's (1967) measurements by lidar also indicated that the concentration inside a plume reached 3 mg m^{-3} in a 200-ft thick layer, showing that it was about two orders of magnitude larger than normal conditions. If Tokyo smog contains considerable numbers of particles in excess of 10 to 20 microns, our assumption of gray smog may not be too far from realistic.

Under the further assumption that the transmissivity inside the smog decreases exponentially as

$$\tau^{\bullet} = e^{-k\Delta P \sec\eta} \tag{11}$$

where $\tau^{\bullet}$ denotes the transmissivity in the direction of nadir angle η, ΔP, the pressure difference at the top and the bottom of the smog which attenuates the radiant energy. Then we define the smog according to its absorptivity $\alpha^{\bullet}$ when radiation penetrates vertically through a 100-mb depth, thus:

$$(1-\alpha^{\bullet}) = \tau^{\bullet} = e^{-100k} \tag{12}$$

where k should be expressed in mb^{-1} units. If we designate graybody smog as No. 1, 2, 3,..., and 9 according to its absorptivity $\alpha^{\bullet}$= 0.1, 0.2, 0.3,..., and 0.9, respectively, the corresponding values of k are 1.06, 2.23, 6.93, ... and 16.09 in $10^{-3}mb^{-1}$ units. A blackbody smog or No. 10 smog is, therefore, characterized by $\alpha^{\bullet}$ = 1.0 or k = infinity.

In order to find out the influence of smog upon T_{BB} measured from various altitudes, T_{BB} was computed for the cases of no smog, smog No. 2, 5, and 8. The results in Fig. 14 reveal that T_{BB} decreases rather rapidly as the aircraft height inside the smog increases. The rate of decrease, as expected, becomes pronounced as the smog number increases. In the case of a blackbody smog, T_{BB} and the smog temperature should coincide.

Of importance is the contribution to the radiation from the ground upon the effective radiant emittance measured at the various aircraft altitudes. We define the ratio

$$\overline{M}_{(h,\eta)} = \frac{\overline{W}_{s(h,\eta)}}{\overline{W}} \tag{13}$$

where $\overline{W}_{s(h,\eta)}$ denotes the effective radiant emittance of the surface reaching the airborne radiometer after passing through the atmosphere including moisture and smog, $\overline{W}$, the total effective radiant emittance, and $\overline{M}_{(h,\eta)}$, the ratio which may be called the "mixing ratio of surface radiation". It should be noted that the surface temperature can be related uniquely to the measured $\overline{W}$ only if $\overline{M} = 1$.

The right-side diagram in Fig. 14 shows the decrease in the relative contribution of the ground as the height and the smog number increases. Due to the radiation from water vapor below the flight level $\overline{M}$ decreases to about 60% when measured from 700 mb without smog. If smog behaves as a blackbody, $\overline{M}$ will be zero at all altitudes, indicating that we are not able to determine the radiative characteristics of the ground from aerial measurements.

It would be difficult to obtain the radiative characteristics of the smog over Tokyo when our radiation measurements were made on July 28, 1968. However, the pattern of T_{BB} in Fig. 13 may reveal the smog conditions under discussion. An attempt was made, therefore, to obtain a large number of computed T_{BB} patterns by changing both the smog numbers and the surface temperatures. A combination of 1 through 9 smog numbers and the surface temperatures 34 through 44C at 2C intervals was studied carefully leading to the conclusion that the surface temperature of 38C combined with No. 2 smog ($\alpha^* = 0.2$) gives the closest pattern to that of the measured one.

The best-fit pattern thus obtained is presented in Fig. 15. The figure shows that the layer of smog No. 2 attenuates the radiation from the ground, resulting in a 4.6C reduction when measured vertically from the smog top. The corresponding reduction without smog is computed to be 3.0C. The lapse rate of T_{BB} above the smog layer is relatively small showing only about 0.6C per 1000 ft.

5. Damping Factor and Crossover Temperature

Due to the fact that the effective radiant emittance reaching a radiation sensor

always includes the atmospheric radiation, the equivalent blackbody temperature corresponding to the measured $\overline{W}$ differs from the surface temperature. By computing a large number of model atmospheres Wark, Yamamoto, and Lienesch (1962) showed a statistical result that the satellite-measured T_{BB} from the 8-13 micron channel is almost always lower than the surface temperature. Our results obtained from airborne measurements also show a significant reduction in the measured T_{BB} as the height increases, except near the altitude of temperature inversion.

Since the difference between T_{BB} and the surface temperature is a result of the fractional contribution of the atmospheric radiation to the total effective radiant emittance, the atmosphere will also reduce the variation in the surface temperature. In other words, the variation, both in time and space, in the surface temperature measured through the atmosphere decreases as the aircraft altitude increases.

We shall now define the damping factor, D, as follows:

$$D = \frac{\Delta T_{BB}}{\Delta T_s} \tag{14}$$

where T_{BB} denotes the measured value, T_s , the surface temperature, and Δ , their variation. The surface may be the ground, the sea surface, etc., as long as it emits as a blackbody.

In order to determine the damping factor over Sagami Bay, the sea-surface temperature was changed from 20 to 30C at 2C intervals while keeping the overlaying atmosphere unchanged. In reality, however, the low-level atmosphere would be modified due to air-sea interaction. Nevertheless, such a condition could exist where a uniform airmass stays over the sea surface characterized by a tight temperature gradient or by areas of local hot and cold spots. Figure 16 shows the variations of T_{BB} thus computed. The input air temperatures and mixing ratios appear to the left at 20-mb intervals. The figure reveals that the damping factor, 77% at 500 m decreases to 51% as the height increases to beyond 5 km. From the satellite level, a damping factor of 50 % should be assumed in this case.

In view of such low values in the damping factor, it is necessary to correct the measured ΔT_{BB} over a small region in order to obtain the thermal gradient over the

sea surface. This fact necessitates a large correction unless an aircraft flies less than 100 ft above the surface for which the damping factor would be about 90%. For a high-level flight necessary to achieve a large-area scan, we must know the thermal characteristics of the atmosphere below the flight level so as to perform required corrections afterward.

The damping factor over Tokyo was computed under various smog conditions by increasing the aircraft altitude up to 10 km. The result in Fig. 17 shows the obvious effects of smog, which increase with the absorptivity α^* . The damping factor of 0.64 applicable to the case without smog is reduced to 0.28 for smog No. 5 and further to 0.11 for smog No. 8, suggesting that only about 10% of the temprature variation at the surface will be measured from the 10-km level when the city is covered with a dense smog. Included also in the figure is the damping factor over the bay and over Arizona computed from the results by Combs et.al. (1965). There are no simple ways of estimating the damping factor as a function of the height and the nadir angle unless the radiative transfer equation is solved numerically taking into consideration the temperature and the humidity distribution inside the atmosphere as well as the temperature of the surface and smog conditions.

In order to convert the equivalent blackbody temperature, T_{BB} measured from an aircraft into a corresponding surface temperature, T_s , we rewrite Eq. (14) into

$$D = \frac{T_{BB} - T_{co}}{T_s - T_{co}}$$

or

$$T_s = T_{co} + (T_{BB} - T_{co}) D^{-1} \tag{15}$$

where T_{co} is a specific temperature satisfying the condition that $T_s = T_{BB} = T_{co}$ when measured from a given aircraft height and nadir angle. The temperature, T_{co} , may be called the "crossover temperature".

Figure 18 was prepared for further explanation of the crossover temperature. The figure shows a computed result that T_{BB} of various surface temperatures measured through a specific atmosphere from $h_a = 3000'$ with a nadir angle of $\eta = 0$ increases with T_s . The mode of increase in T_{BB} is more or less linear, crossing the straight line of T_s at a point indicated by a black circle at which T_{BB} and T_s are equal. The circle denotes the crossover point of two lines and the temperature at the circle is the

crossover temperature. The tangent of the T_{BB} line represents obviously the damping factor, D, which can be measured on the diagram. Rigorously, of course, the damping factor, D, as defined by Eq.(14) is not necessarily a constant. This is reflected in the slight curvature of the T_{BB} line in Fig. 18.

It is important to note that both T_{CO} and D under given atmospheric and smog conditions are, respectively, a function of both aircraft height, h_a and the nadir angle of view, η . Thus the surface temperature from Eq. (15) can be computed for given vertical distributions of temperature, water vapor, and smog or other assumed-graybody matter after expressing T_{CO} and D as functions of h_a and η.

6. Examples of Temperature Measurements over the Tokyo Area

About ten locations of temperature measurements were selected in an attempt to determine surface temperatures at these locations. Due to the fact that the variation of surface temperature is far more dramatic than that of air temperature, we selected several scan spots inside each predetermined location.

Although only three aircraft altitudes, 1000, 2000, and 3000 ft were used in our experiment, equivalent blackbody temperatures were computed for the altitudes at 1000 ft intervals up to 8000 ft. The nadir angle of view was kept at 45° since this angle was found to be most convenient in aiming a hand-held PRT-4 radiometer. Shown in Fig. 19 are the crossover temperatures and the damping factor for each altitude. It will be found that the variations in T_{BB} when measured from about 2500 ft should practically be doubled when converted into T_S . We are, of course, assuming that the atmospheric stratification over the Tokyo area is uniform. This assumption might not be true. As long as the radiative property of the atmosphere is concerned, however, expected irregularities are negligible in comparison with much greater variation in the radiant emittance of surfaces radiating under the midsummer sun.

Figures 20 and 21 show six locations of T_{BB} measurements and recorded traces scaled in both T_{BB} and T_S . The latter was computed from Eq. (15) by using the values of T_{CO} and D in Fig. 19.

Ginza Avenue was scanned from 1000 ft, first looking west pointing toward the sides of buildings heated by the morning sun, then looking east toward the sides which have started receiving the afternoon sunlight. Due partially to choppiness caused by

a low-altitude flight and also to the large structure on Ginza, no clear-cut temperature patterns were obtained. It may be stated, however, that the avenue in the shade shows a cool 34C while some building tops are quite hot, say 44C.

At the Japan Meteorological Agency (JMA), temperatures of asphalt and soil surfaces were measured at one-hour intervals during our flight started shortly before sunrise and ended in midafternoon. The variations in surface and air temperatures as well as those of wind and clouds are presented in Fig. 22. At 1025 JST when measured surface and air temperatures were about 41 to 45C and 31C, respectively, the shady side of JMA was 37C (T_{BB} = 34C) and the sunlit side, 42C (T_{BB} = 36C). Then the radiometer was pointed toward the Imperial Moat with shallow water to obtain 32C (T_{BB} = 30C). These temperatures seem to be quite reasonable when compared with the ground measurements. It should be pointed out that the measured T_{BB} are far from actual T_S , thus necessitating proper corrections in order to calculate T_S from T_{BB} obtained indirectly from aircraft.

Meiji Shrine is surrounded by woods with trees 70 to 130 years old. An arc-shaped scan with a short pause when pointing toward the shrine building was made at 1330 JST obtaining 33 to 37C tree-top temperature. A 44C temperature of the building with copper roofs renewed in 1958 seems to be several degrees lower than expected. It is very likely that the half-power scan spot, an ellipse of 100 x 150 ft axes, was too large to be kept on the roof while a short pause was attempted. Moreover, the full-power scan spot is expected to be several times larger than the integrated areas of copper roofs. When the scan spot moved out into a residential area just outside the shrine, the estimated surface temperature increased to 46C with a peak maximum reaching 48C.

The Sumida River and several bridges were scanned with a short pause at each bridge crossing. The scan spot was placed in the river north of Azuma Bridge, obtaining a 31C water temperature. Two 39C peaks were recorded while crossing Azuma and Komagata Bridges. The third bridge showed a 37C temperature followed by a 30C water temperature. When the scan spot was moved to the river bank, T_S increased to 43C.

Harumi Pier with warehouses on the waterfront was scanned from 3000 ft in such a manner that the scan spot was moved alternately from the water to the land. A temperature difference of about 12C was obtained. The lowest water temperature of 26C appeared at the time when the over-water scan started.

Enoshima Beach crowded with people was scanned at 1500 JST, the hottest time of the day. The spot was moved off-shore until the entire full-power scan spot moved into the water with breaking waves, then it was brought back to the sandy beach. Such a motion of the scan spot resulted in an average of 31C water temperature and 40C sand-beach temperature. We expected to obtain much higher surface temperatures from the beach where one would feel much higher temperatures while walking barefoot.

These examples of the surface-temperature estimated from airborne measurements of T_{BB} indicate that it is feasible to determine surface temperature very efficiently. The estimated values agree mostly with those measured on the ground and also with those expected on a midsummer day.

7. Conclusions

The experimental results of airborne infrared measurements over the slope of Mt. Fuji, Sagami Bay, and Tokyo revealed that a 8-13 micron radiometer is capable of measuring equivalent blackbody temperatures from various surfaces radiating at different temperatures. Due to atmospheric absorption and concurrent reradiation, however, the measured equivalent blackbody temperatures are far from the temperatures of the radiating surfaces which may be assumed to be blackbody radiators for most practical purposes.

Since the amount of temperature correction applied to the equivalent blackbody temperature is a function of the surface temperature to be estimated, it is necessary to obtain two parameters introduced in this paper. They are D, the damping factor, and T_{CO} , the crossover temperature. Using these parameters, we are able to determine surface temperatures within an area over which the radiative properties of the atmosphere may be assumed uniform.

The examples of measurements and a correction method proposed in this paper will increase the accuracy of estimating the surface temperatures through indirect sensing of the effective radiant emittance in the 8-13 micron region.

A next logical step in further verification of these results is to apply them to problems such as the determination of sea-surface temperature from satellite and airborne radiometers, mapping of hot and cold spots over a vast heated plane, determination of water pollution by mapping the midday surface temperatures, etc. It will

even be possible to determine the degree of air pollution if we measure the equivalent blackbody temperature of a surface of known temperature.

ACKNOWLEDGEMENTS:

The authors are very grateful to the Asahi Newspaper for giving us ample flight time for the completion of our measurements. Acknowledgements are also due to Mr. Koichi Simizu of Asahi Sansho, who made a successful inflight recording of the radiation data used in this research and to Dr. Atsushi Kurashima for his kind efforts to initiate and carry out this experiment.

REFERENCES

Barret E.W. and O. Ben-Dov (1967): Application of the lidar to air pollution measurements. J. App. Meteor., 6, 500-515.

Combs, A.C., H.K. Weickman, C. Mader, and A. Tebo (1965): Application of infrared radiometers to meteorology. J. App. Meteor., 4, 253-262.

Greenfield, S.M. and W.W. Kellogg (1960): Calculations of atmospheric infrared radiations as seen from a meteorological satellite. J. Meteor., 17, 283-290.

Japan Meteor. Agency (1958): Fuji-san no kisho (Weather at the summit of Mt. Fuji) Special Volume giving the results of observations along the mountain slope. pp. 79.

Lenschow, D.H. and J.A. Dutton (1964): Surface temperature variations measured from an airplane over several surface types. J. App. Meteor., 3, 65-69.

Lorenz, V.D. (1967): Temperaturmessungen von Boden- und Wasseroberflächen von Luftfahrzeugen aus. Pure and Applied Geophysics, 67, 197-220.

NASA (1961): TIROS II Radiation data users' manual. Goddard Space Flight Center, Greenbelt, Md..

Pueschel, R.F. and K.E. Noll (1967): Visibility and aerosol size frequency distribution. J. App. Meteor., 6, 1045-1052.

Wark, D.Q., G. Yamamoto, and J.H. Lienesch (1962): Methods of estimating infrared flux and surface temperature from meteorological satellites. J. Atm. Sci., 19, 369-384.

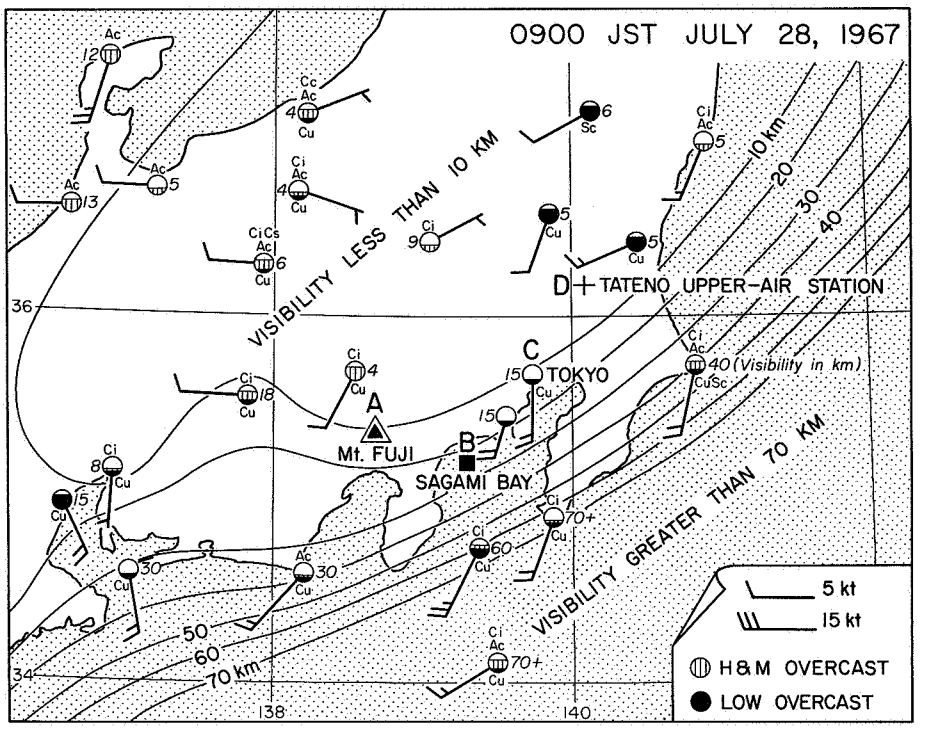

Fig. 1. Surface chart showing the distribution of clouds and visibility at 0900 JST July 28, 1967, the day of radiation measurements over Mt. Fuji, Sagami Bay, and Tokyo.

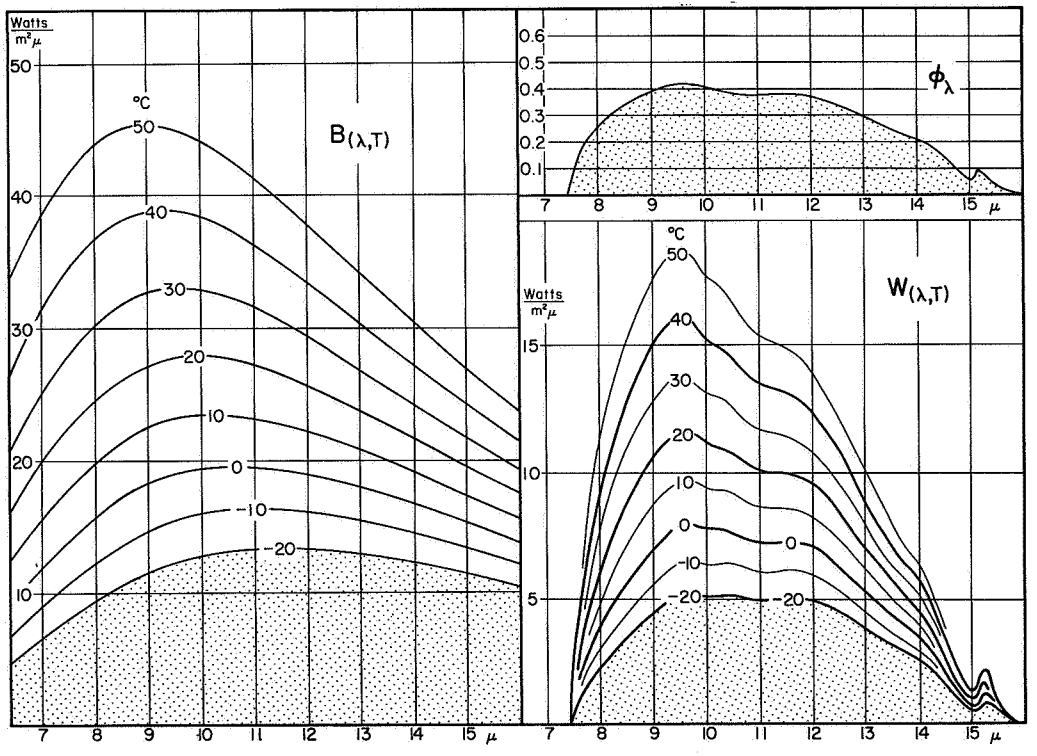

Fig. 2. The Planckian radiant emittance between -20 and 50C and the spectral radiant emittance obtained by multiplying by the spectral response, ϕ_λ of a Barnes PRT-4 shown in the upper right diagram.

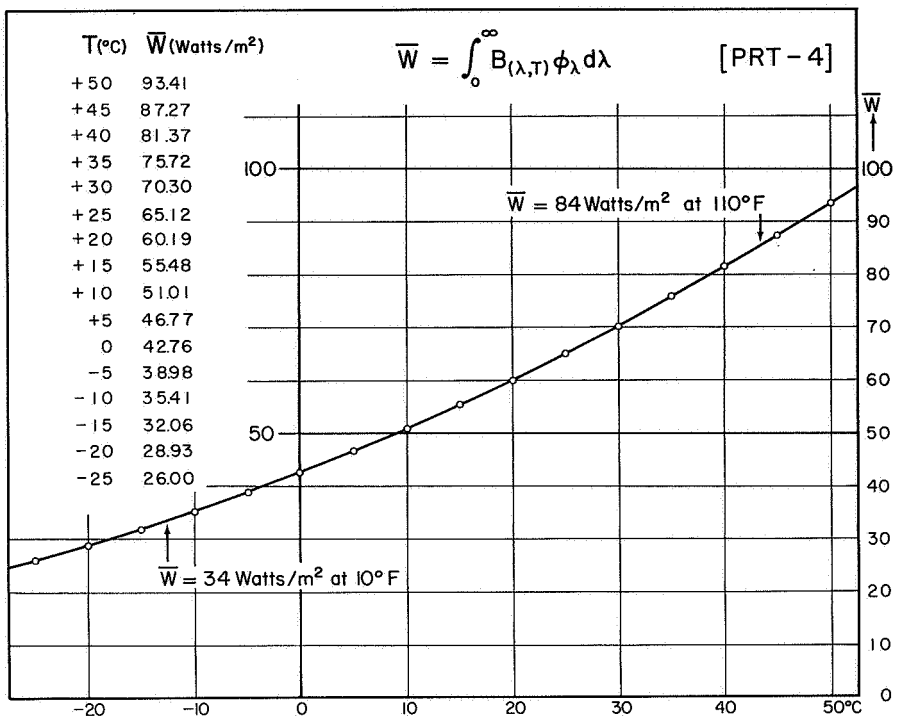

Fig. 3. The effective radiant emittance of a Barnes PRT-4 radiometer. About 40C chopper temperature of the unit used in this experiment was so low that the output reading in m V showed a reversed response when the radiometer was calibrated on the ground by pointing it toward hot objects heated by the sun.

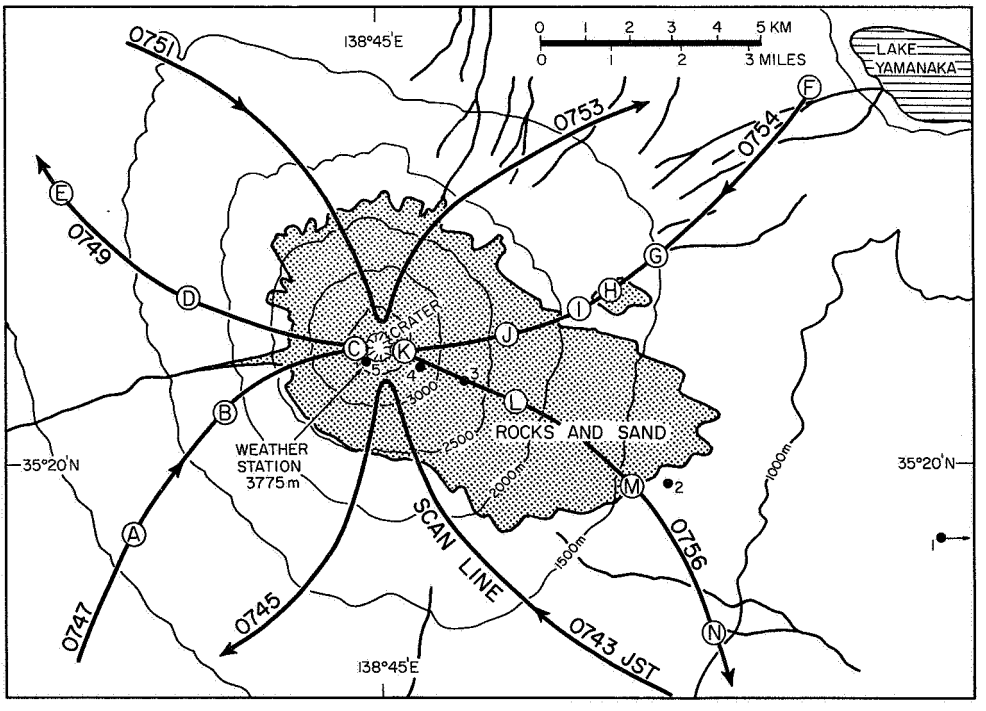

Fig. 4. Four scan lines on the slope of Mt. Fuji, a 3776 m (12,886 ft) volcano. These scans were made on July 28, 1967 from an aircraft at 12,000 ft while circling the peak keeping a radius of about 13 km. The stippled areas are the ground with loose rocks and sand mostly free from trees.

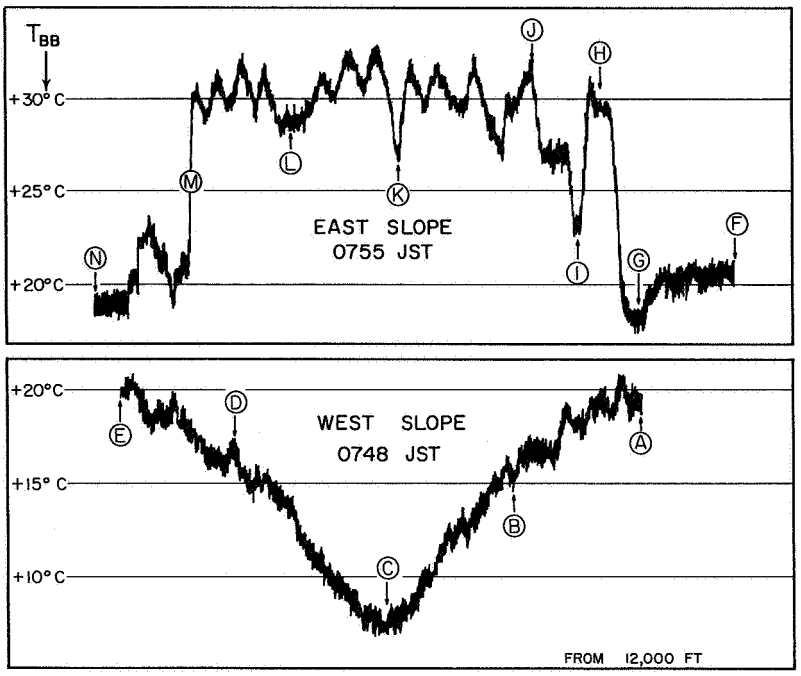

Fig. 5. Examples of recorded traces obtained from the east slope (upper) and the west slope scanning. About 2 min were spent in completing a V-shaped scan. Horizontal lines represent the equivalent blackbody temperatures without corrections due to water-vapor absorption. Date: July 28, 1967.

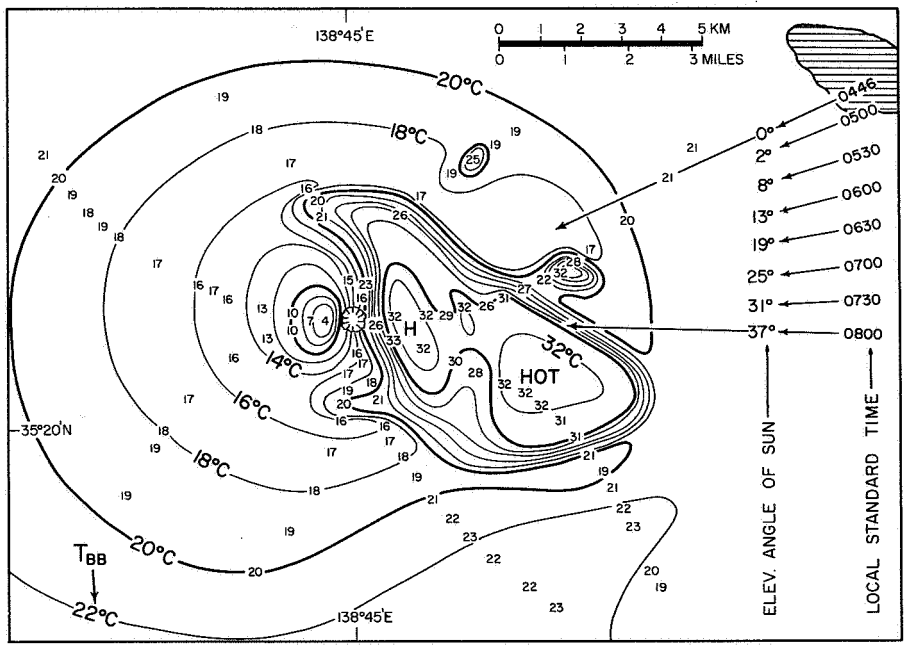

Fig. 6. Distribution of the equivalent blackbody temperature obtained by the PRT-4 radiometer between 0743 and 0756 JST, July 28, 1967. The distance from the aircraft to the scan spots varies between 5 and 15 km, resulting in a variation of the scan-spot size between about 150 and 500 m in diameter. The azimuth and the elevation angle of the sun in the figure show that the east slope has been heated since 5 am.

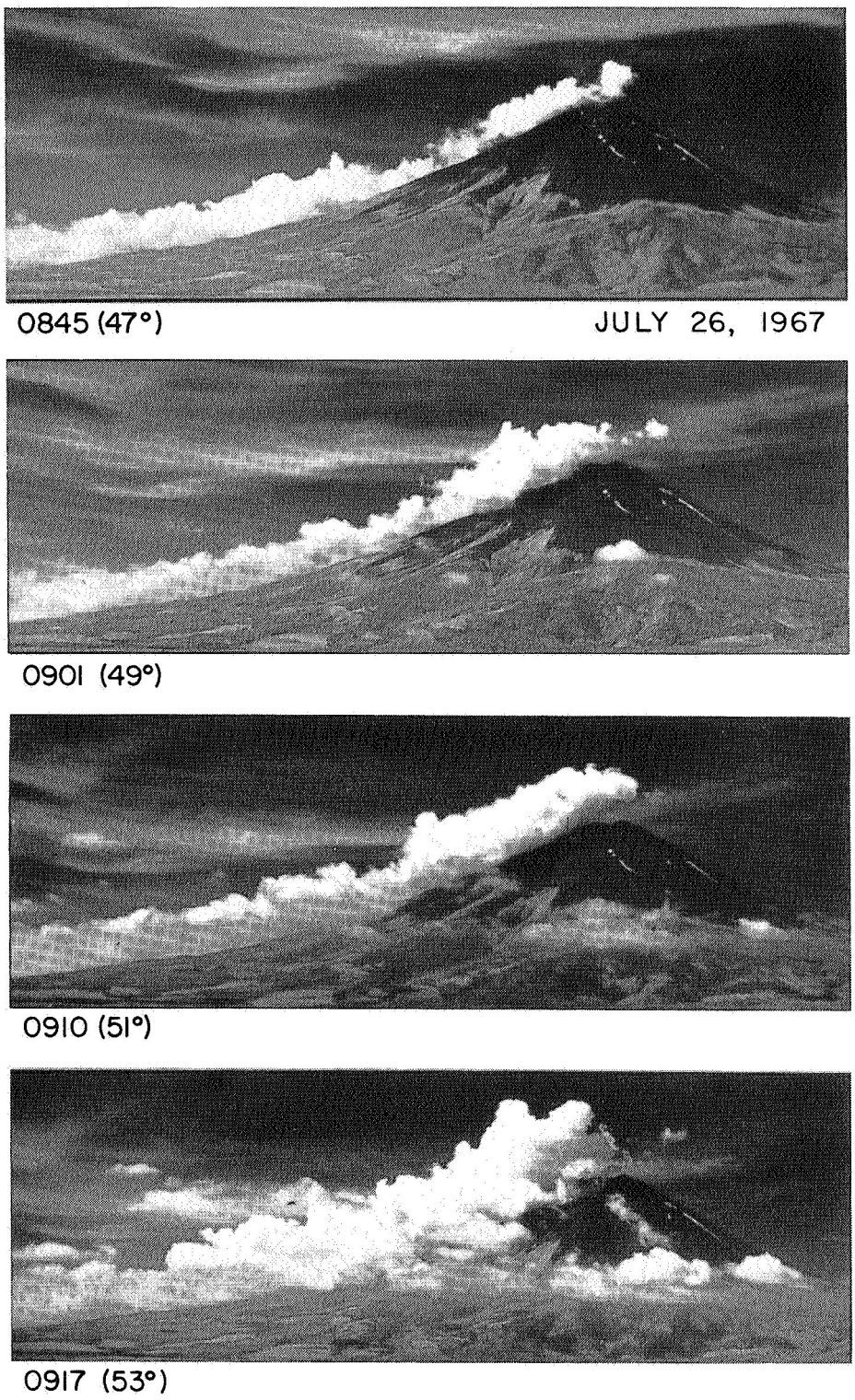

Fig. 7. Stages of the formation of cumulus clouds along the east slope of Mt. Fuji. Pictures were taken from Funatsu Weather Station on July 26, 1967, two days before the radiation measurements. (courtesy of Mr. Saburo Yamamoto and Yadoru Yuyama.)

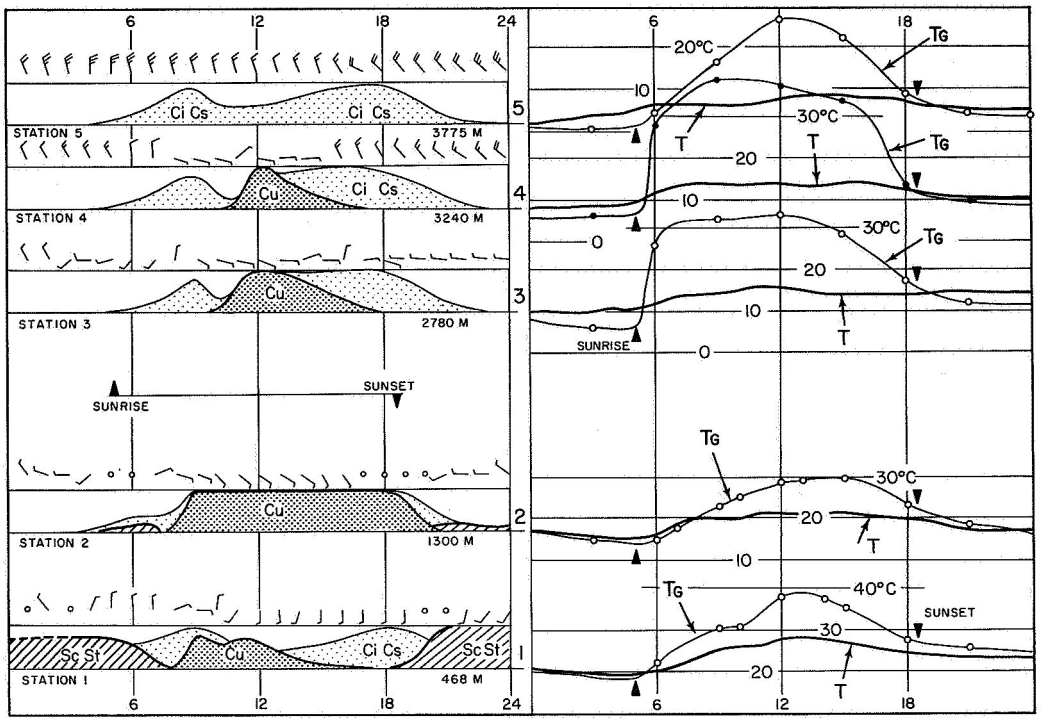

Fig. 8. Time cross sections of meteorological parameters observed at five stations along the east slope of Mt. Fuji. T_G denotes the ground temperature, T, the air temperature measured inside the instrument shelter, and black triangles, the times of sunset and sunrise.

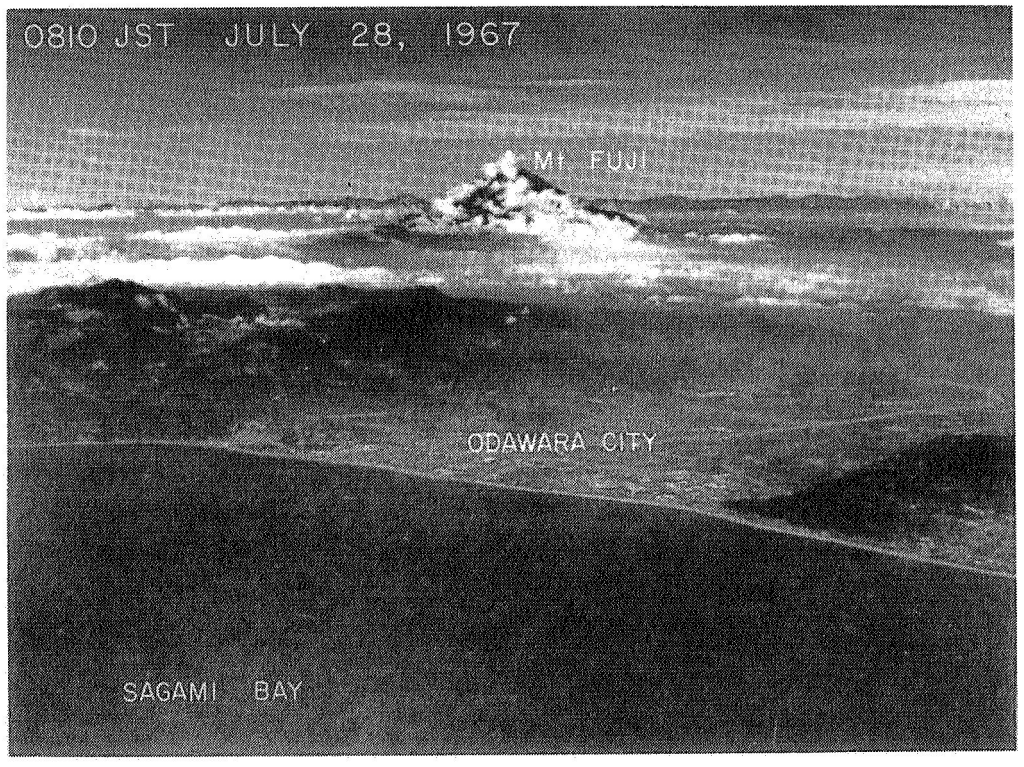

Figure 9. The Sagami Bay area where the nadir angle and the height dependence of T_{BB} were obtained. Note that the east slope of Mt. Fuji is covered with scattered cumuli.

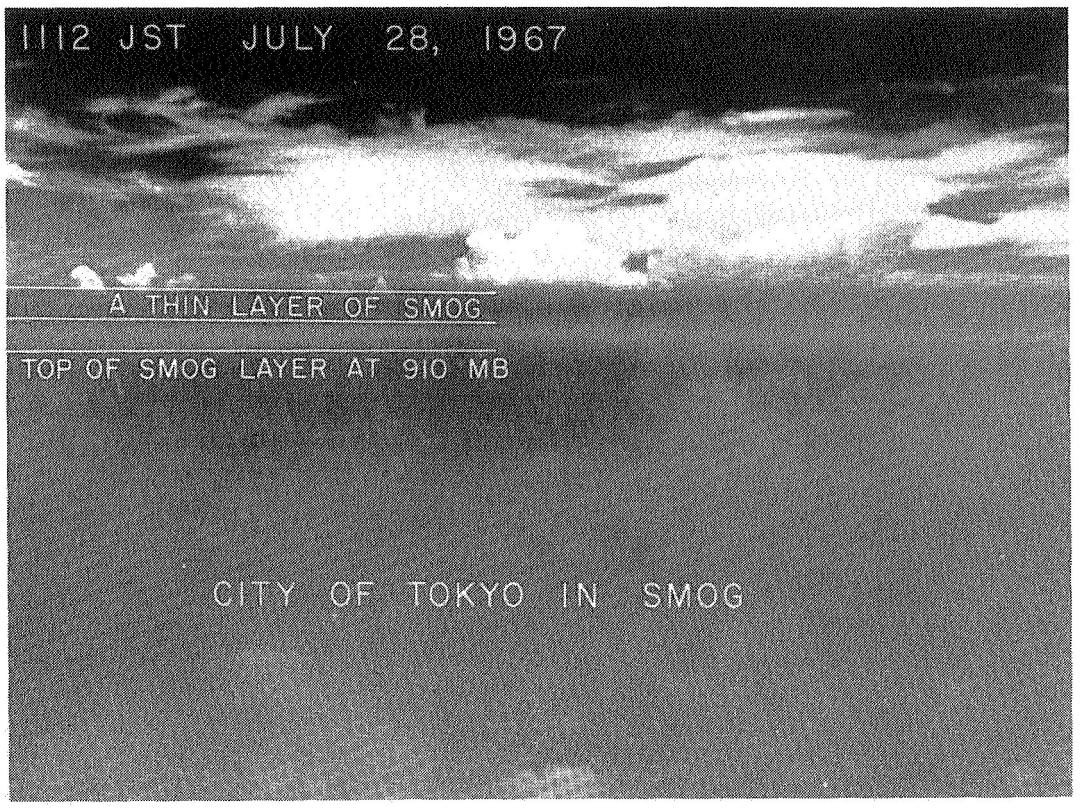

Fig. 10. The western part of Tokyo where radiation measurements were made by changing both nadir angles and flight levels. The city was covered with a light to moderate smog. The air above the smog top was very clean.

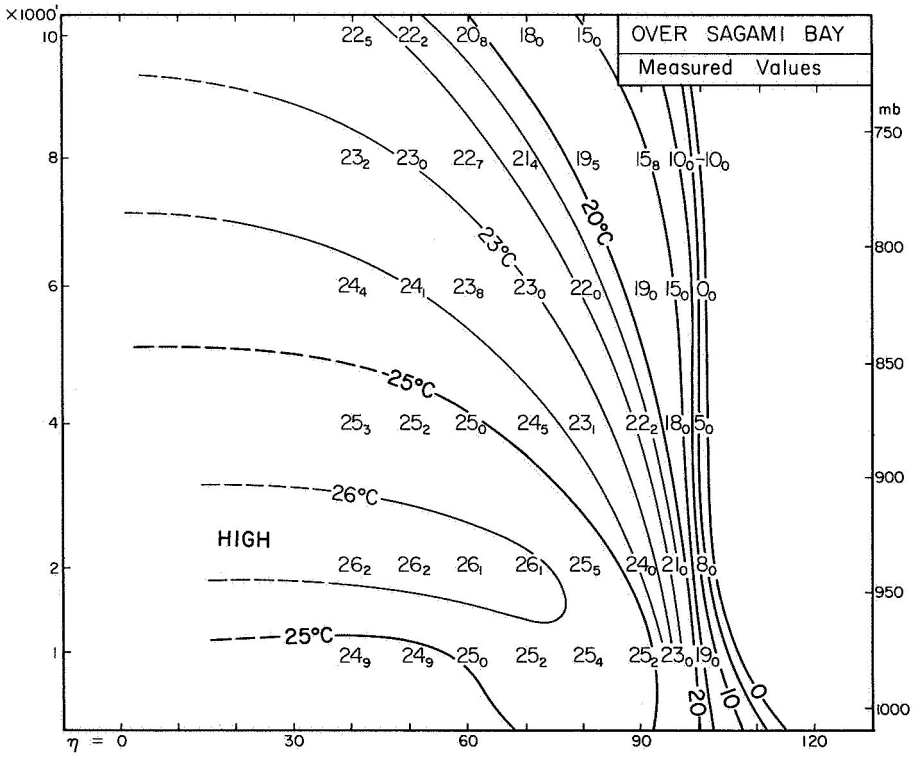

Fig. 11. Patterns of T_{BB} measured over Sagami Bay between 0811 and 0843 JST July 28, 1967. The sea-surface temperature is extrapolated to be about 24.5 C.

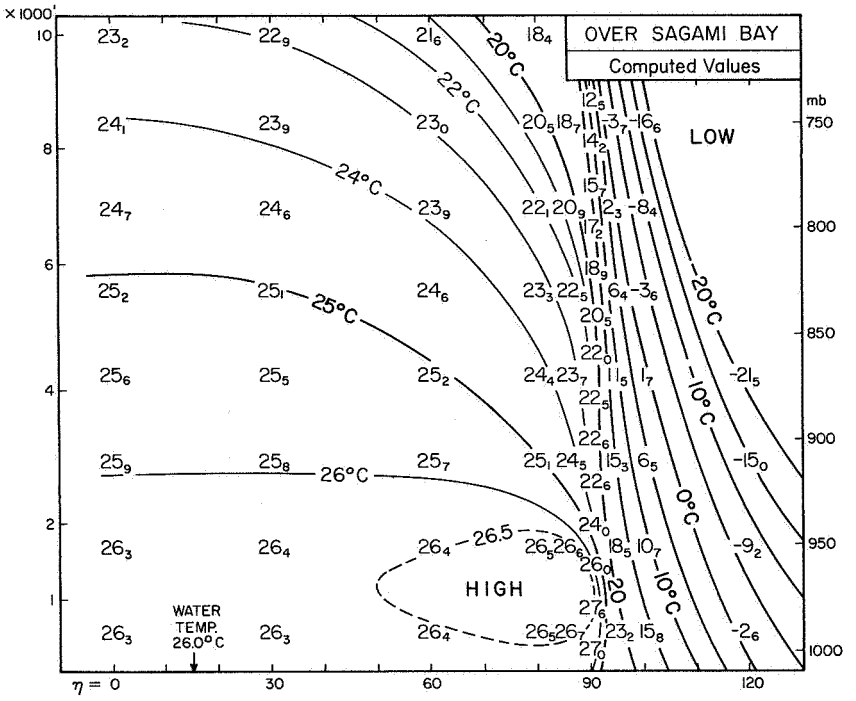

Fig. 12. Computed patterns of T_{BB} . The sea-surface temperature of 26.0C and the air temperatures entered along the vertical through $\eta = 90°$ were used as input data.

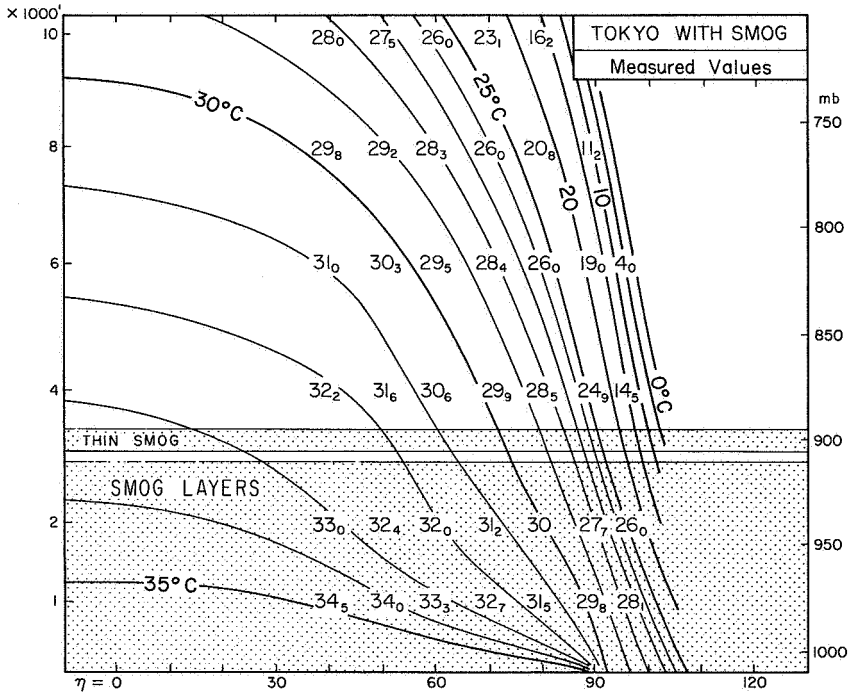

Fig. 13. Patterns of T_{BB} measured over Tokyo between 1115 and 1142 JST July 28, 1967. The levels of smog layers over the city are stippled.

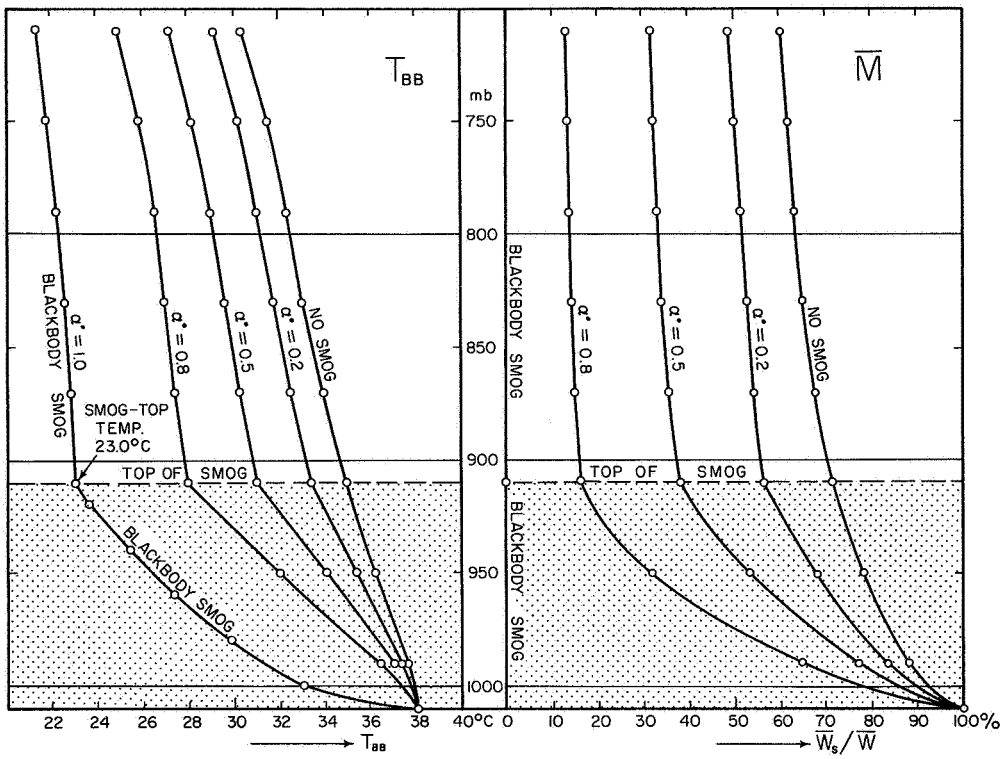

Fig. 14. Decrease in T_{BB} measured downward from various altitudes scaled in mb. (left). The density of smog was changed from transparent to the blackbody smog. Mixing ratio of surface radiation, $\overline{M}$ also decreases as the flight level increases. Note that the blackbody smog gives $\overline{M} = 0$ at all altitudes.

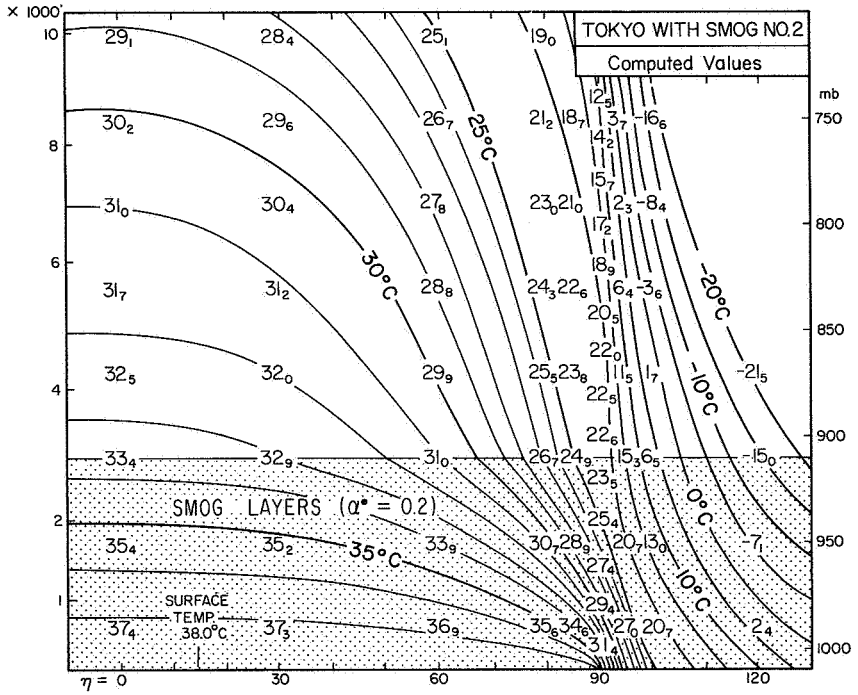

Fig. 15. The best fit patterns of T_{BB} over Tokyo obtained by introducing a smog of 0.2 absorptivity when looking down through a 100-mb atmosphere.

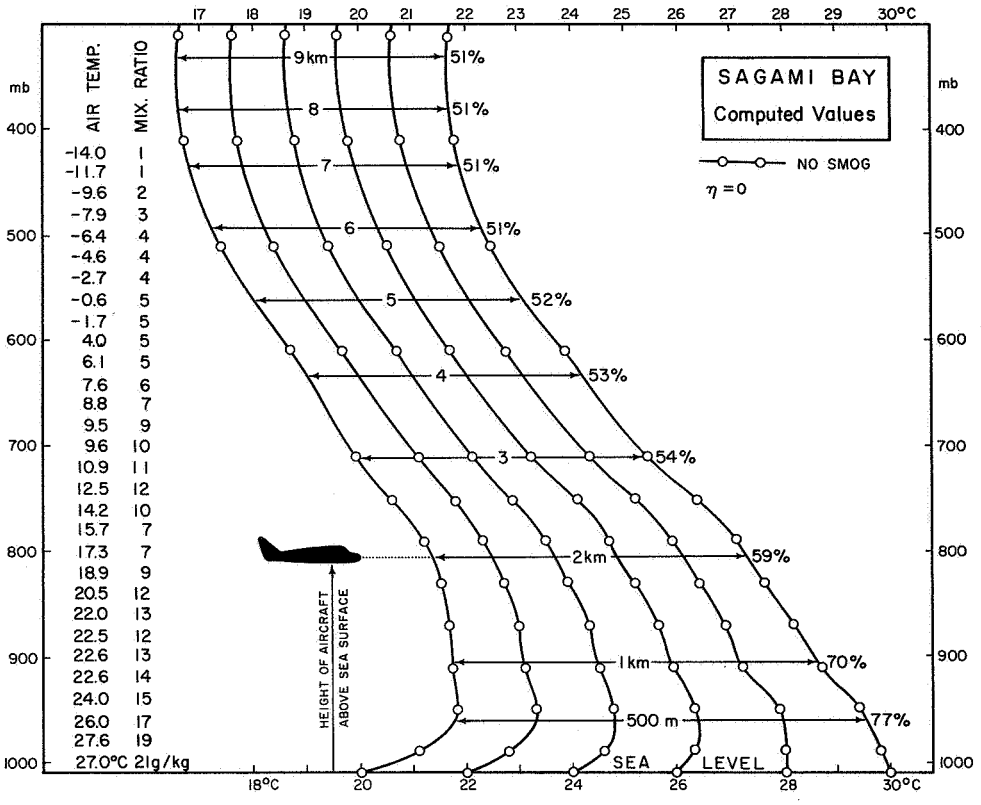

Fig. 16. Change in T_{BB} of six targets measured from various altitudes up to 10 km. The temperature and the mixing ratio of the atmosphere were kept unchanged while the target temperatures were increased from 20 to 30C at 2C intervals.

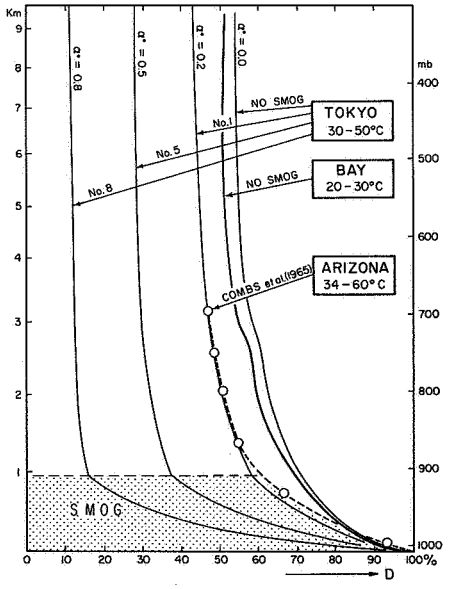

Fig. 17. Decrease in the temperature damping factor, D, as a function of the aircraft height above the radiating surface. The values were computed at zero nadir angle. One case without smog and three cases of varying smog over Tokyo indicate that smog damps the surface-temperature variations measured by an airborne radiometer.

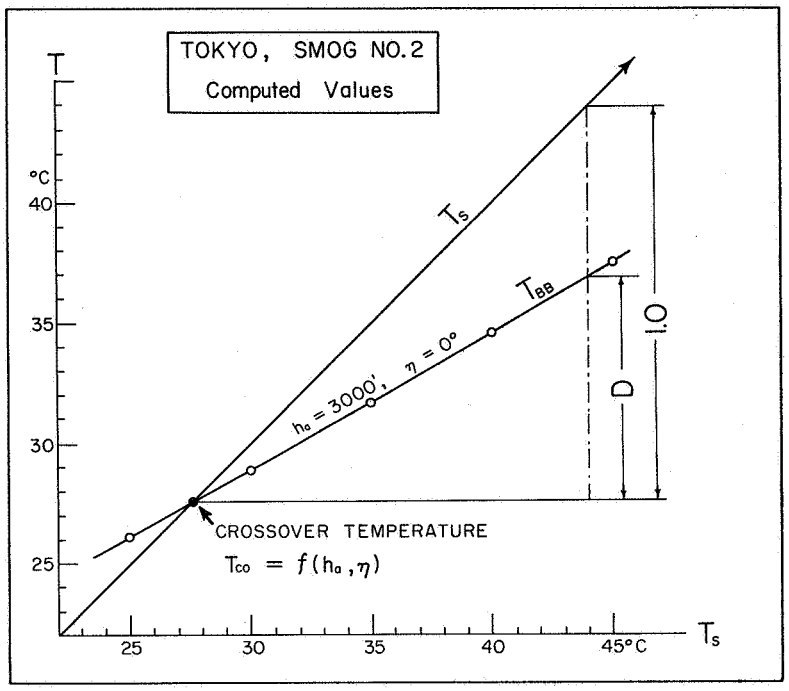

Fig. 18. A diagram for computing the crossover temperature, T_{co}, and the damping factor, D, from computed values of T_{BB}. Tokyo with smog No. 2 was used for the computation while changing the surface temperature from 25 to 45 C at 5C intervals.

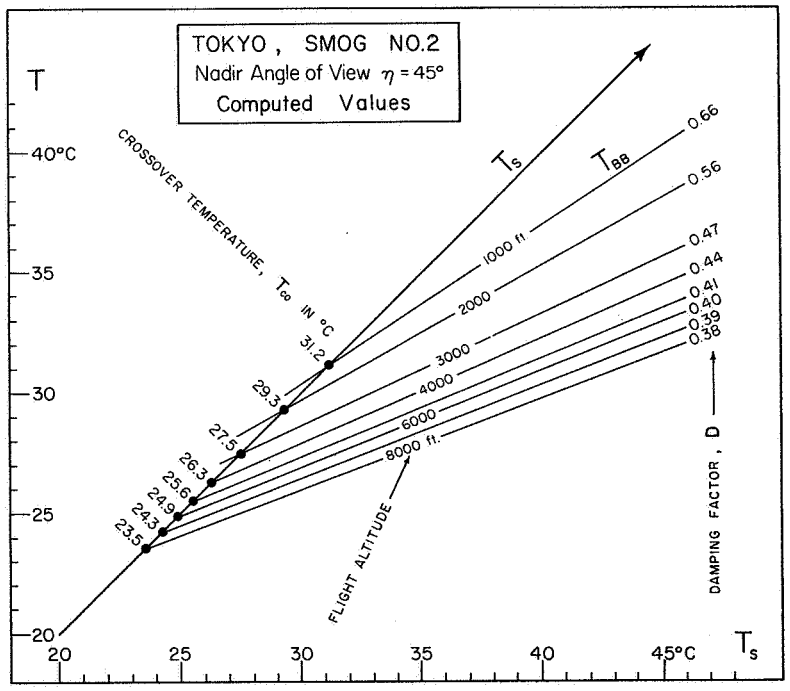

Fig. 19. Crossover temperatures and damping factors computed for a 45° nadir angle of view from aircraft altitudes between 1000 and 8000 ft. These values were used in estimating surface temperatures from equivalent blackbody temperatures measured over Tokyo on July 28, 1967.

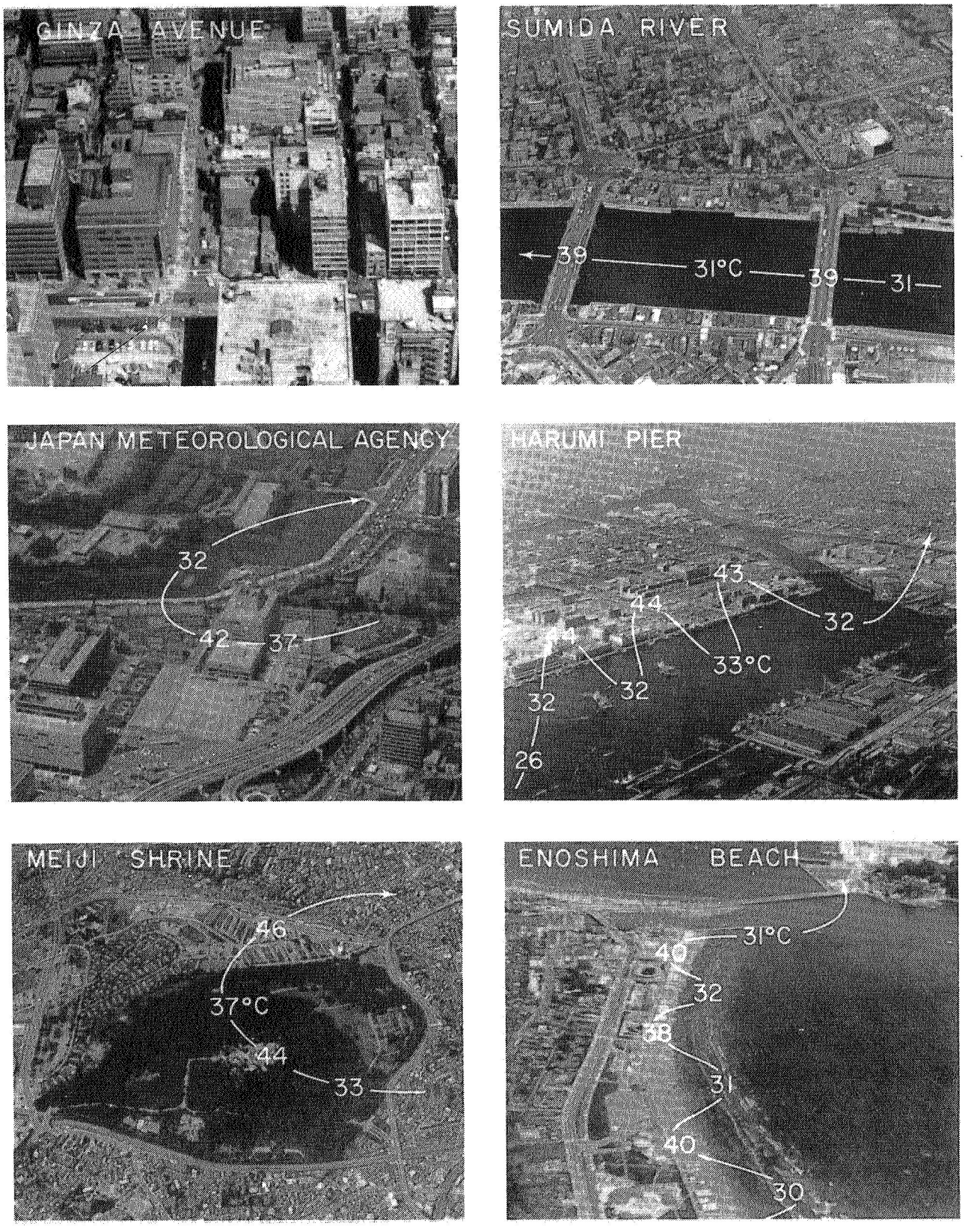

Fig. 20. Scan lines and surface temperatures superimposed upon aerial pictures taken on July 28, 1967, the day of radiation measurements. Pictures are: Ginza Avenue looking east, Japan Meteorological Agency and a portion of the Imperial Moats, Meiji Shrine surrounded by extensive woods, Sumida River with Komagata and Azuma Bridges near Asakusa, Harumi Pier and Sumida River, and a beach opposite from Enoshima.

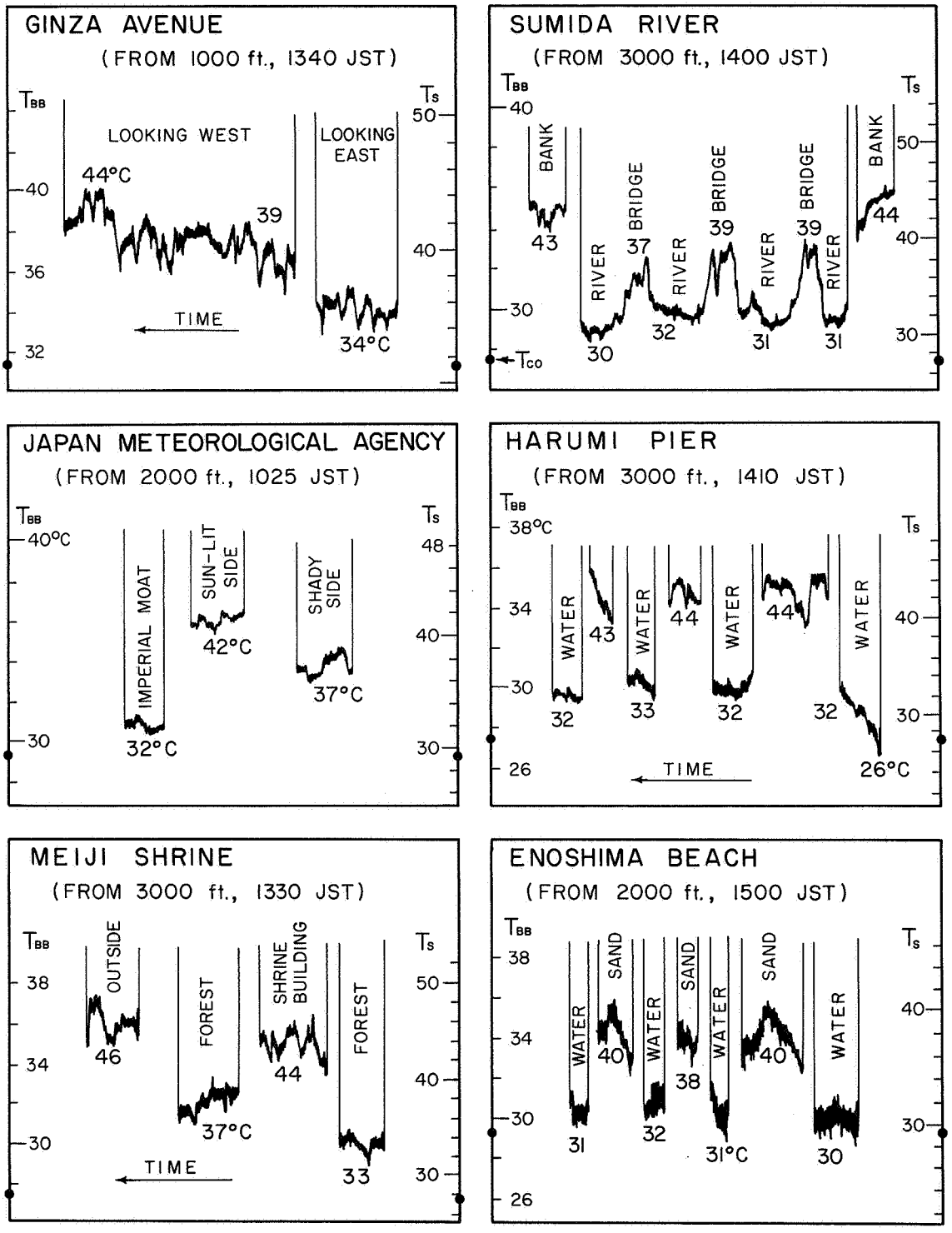

Fig.. 21. Recorded traces obtained from six locations in the previous figure. The radiometer's field of view was obstructed by the observer's hand when the scan spot was moved from one object to the next. The temperature scale to the left indicates T_{BB} while the other one to the right is the surface temperature, T_S , computed from Eq. 10 and values of T_{CO} and D in fig. 19.

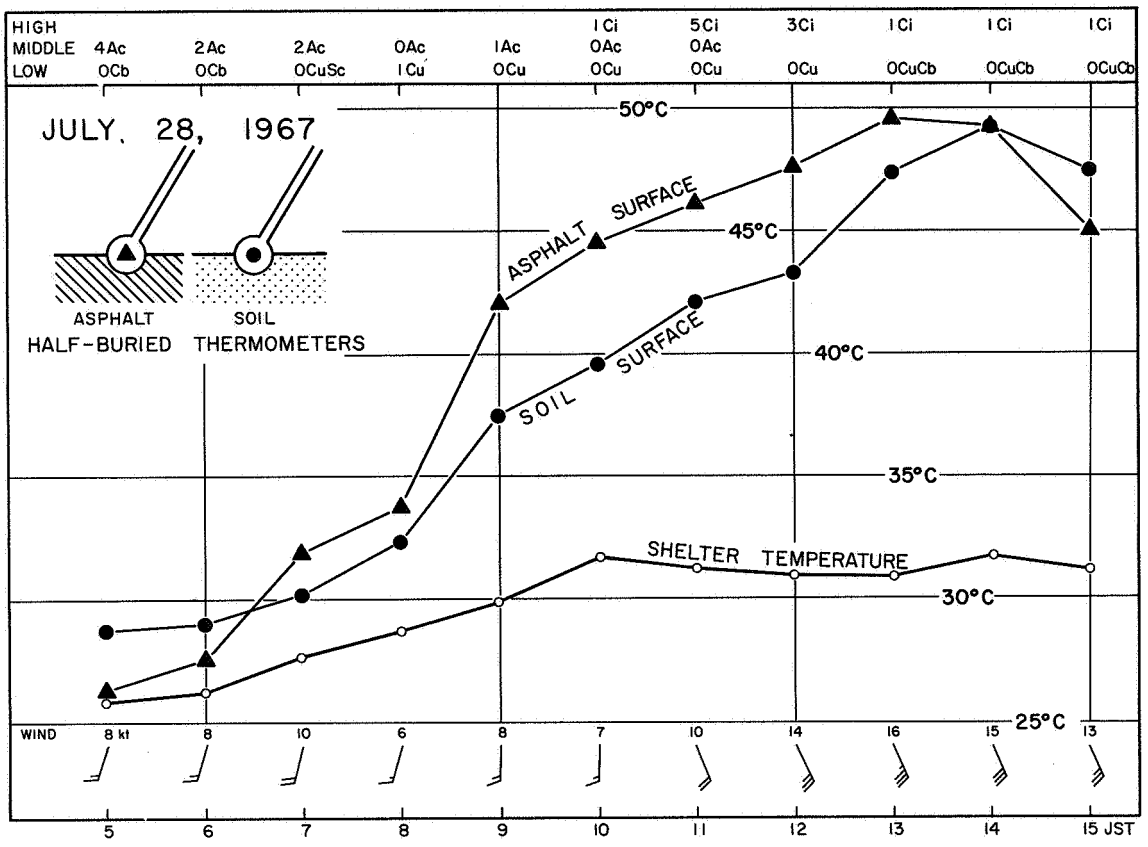

Fig. 22. Change in the surface and the air temperature at the Japan Meteorological Agency located near the northeast corner of the Imperial Palace. Note that surface temperatures reached almost 50C while air temperatures measured in the instrument shelter were only up to 32C. Shown at the top are types and amounts of clouds.

MESOMETEOROLOGY PROJECT - - - RESEARCH PAPERS

(Continued from front cover)

42. A Study of Factors Contributing to Dissipation of Energy in a Developing Cumulonimbus - Rodger A. Brown and Tetsuya Fujita

43. A Program for Computer Gridding of Satellite Photographs for Mesoscale Research - William D. Bonner

44. Comparison of Grassland Surface Temperatures Measured by TIROS VII and Airborne Radiometers under Clear Sky and Cirriform Cloud Conditions - Ronald M. Reap

45. Death Valley Temperature Analysis Utilizing Nimbus I Infrared Data and Ground-Based Measurements - Ronald M. Reap and Tetsuya Fujita

46. On the "Thunderstorm-High Controversy" - Rodger A. Brown

47. Application of Precise Fujita Method on Nimbus I Photo Gridding - Lt. Cmd. Ruben Nasta

48. A Proposed Method of Estimating Cloud-top Temperature, Cloud Cover, and Emissivity and Whiteness of Clouds from Short- and Long-wave Radiation Data Obtained by TIROS Scanning Radiometers - T. Fujita and H. Grandoso

49. Aerial Survey of the Palm Sunday Tornadoes of April 11, 1965 - Tetsuya Fujita

50. Early Stage of Tornado Development as Revealed by Satellite Photographs - Tetsuya Fujita

51. Features and Motions of Radar Echoes on Palm Sunday, 1965 - D. L. Bradbury and Tetsuya Fujita

52. Stability and Differential Advection Associated with Tornado Development - Tetsuya Fujita and Dorothy L. Bradbury

53. Estimated Wind Speeds of the Palm Sunday Tornadoes - Tetsuya Fujita

54. On the Determination of Exchange Coefficients: Part II - Rotating and Nonrotating Convective Currents - Rodger A. Brown

55. Satellite Meteorological Study of Evaporation and Cloud Formation over the Western Pacific under the Influence of the Winter Monsoon - K. Tsuchiya and T. Fujita

56. A Proposed Mechanism of Snowstorm Mesojet over Japan under the Influence of the Winter Monsoon - T. Fujita and K. Tsuchiya

57. Some Effects of Lake Michigan upon Squall Lines and Summertime Convection - Walter A. Lyons

58. Angular Dependence of Reflection from Stratiform Clouds as Measured by TIROS IV Scanning Radiometers - A. Rabbe

59. Use of Wet-beam Doppler Winds in the Determination of the Vertical Velocity of Raindrops inside Hurricane Rainbands - T. Fujita, P. Black and A. Loesch

60. A Model of Typhoons Accompanied by Inner and Outer Rainbands - Tetsuya Fujita, Tatsuo Izawa, Kazuo Watanabe, and Ichiro Imai

MESOMETEOROLOGY PROJECT - - - RESEARCH PAPERS

(Continued from inside back cover)

61. Three-Dimensional Growth Characteristics of an Orographic Thunderstorm System - Rodger A. Brown.

62. Split of a Thunderstorm into Anticyclonic and Cyclonic Storms and their Motion as Determined from Numerical Model Experiments - Tetsuya Fujita and Hector Grandoso.

63. Preliminary Investigation of Peripheral Subsidence Associated with Hurricane Outflow - Ronald M. Reap.

64. The Time Change of Cloud Features in Hurricane Anna, 1961, from the Easterly Wave Stage to Hurricane Dissipation - James E. Arnold.

65. Easterly Wave Activity over Africa and in the Atlantic with a Note on the Inter-tropical Convergence Zone during Early July 1961 - James E. Arnold.

66. Mesoscale Motions in Oceanic Stratus as Revealed by Satellite Data - Walter A. Lyons and Tetsuya Fujita.

67. Mesoscale Aspects of Orographic Influences on Flow and Precipitation Patterns - Tetsuya Fujita.

68. A Mesometeorological Study of a Subtropical Mesocyclone - Hidetoshi Arakawa, Kazuo Watanabe, Kiyoshi Tsuchiya, and Tetsuya Fujita.

69. Estimation of Tornado Wind Speed from Characteristic Ground Marks - Tetsuya Fujita, Dorothy L. Bradbury, and Peter G. Black.

70. Computation of Height and Velocity of Clouds from Dual, Whole-Sky, Time-Lapse Picture Sequences - Dorothy L. Bradbury and Tetsuya Fujita

71. A Study of Mesoscale Cloud Motions Computed from ATS-I and Terrestrial Photographs - Tetsuya Fujita, Dorothy L. Bradbury, Clifford Murino, and Louis Hull.